Available online at www.sciencedirect.com
ScienceDirect
Trans. Nonferrous Met. Soc. China 35(2025) 3179−3190
Transactions of Nonferrous Metals Society of China
www.tnmsc.cn

Effect of iron content on microstructures and mechanical properties of new ultra-high strength Al−Zn−Mg−Cu alloys

Xin-yuan XU[1], Lei JIANG[1], Xin-biao ZHANG[1], Ming-hong MAO[1], Jian-xin XIE[1,2,3]

1. Beijing Advanced Innovation Center for Materials Genome Engineering, University of Science and Technology Beijing, Beijing 100083, China;
2. Beijing Laboratory of Metallic Materials and Processing for Modern Transportation, University of Science and Technology Beijing, Beijing 100083, China;
3. Key Laboratory for Advanced Materials Processing (MOE), University of Science and Technology Beijing, Beijing 100083, China

Received 7 February 2024; accepted 13 September 2024

Abstract: The impact of Fe content on the microstructures and mechanical properties of an ultra-high strength aluminum alloy, namely, Al−10.50Zn−2.35Mg−1.25Cu−0.12Cr−0.1Mn−0.1Zr−0.1Ti, was investigated. It is found that the increase of Fe content leads to a notable rise in the volume fraction of microscale secondary phases, including (Cu,Fe,Mn,Cr)Al_7, σ phase (composed of Al, Zn, Mg, and Cu elements), and Al_3(Zr,Ti). The formation of these secondary phases results in the depletion of certain phase-forming elements, thereby significantly reducing the quantity of strengthening phases. Fe imposes minimal impact on tensile strength, but it can significantly alter the elongation (δ). For instance, the average elongation of the alloy with 0.18 wt.% Fe (δ=4.5%) is less than half that of the alloy with Fe less than 0.1 wt.% (δ=9.9%−10.9%). The reduction in elongation is attributed to the combined effects of the formation of coarse secondary phases and the diminished quantity of strengthening phases around these coarse phases.
Key words: Al−Zn−Mg−Cu alloy; tensile property; element distribution; secondary phase; Fe content

1 Introduction

The Al−Zn−Mg−Cu alloys, commonly designated as the 7xxx series, are pivotal structural materials in a range of contemporary industries such as transportation and aerospace, due to their exceptional strength, corrosion resistance, favorable processability, and recyclability [1−3]. However, the addition of Fe as an alloying element is known to be deteriorative to the properties of these alloys. During solidification, Fe typically combines with other elements to form secondary phases, which are usually microscale in size. The secondary phases so formed are rather difficult to eliminate through subsequent thermomechanical processing or heat treatment. The presence of Fe-containing secondary phases in the Al−Zn−Mg−Cu alloys largely hinders their practical applications at scale [4].

The secondary phases in these alloys caused by Fe could manifest in varied forms, such as Al_7Cu_2Fe [5], $Al_{17}(Fe_{3.2},Mn_{0.8})Si_2$ [6], $Al_{13}Fe_4$ (or Al_6Fe) [7], $(Al,Cu)_6(Fe,Cu)$ [8], $Al_{23}CuFe_4$ [9,10], Al_3Fe [10], (Cu,Fe,Mn)Al_3 [11], and (Cu,Fe,Mn,Cr)-Al_7 [11]. The formation of these secondary phases depletes the dispersion strengthening elements in the alloy matrix such as Cu, Cr, and Mn, and in turn degenerates the key properties such as ductility and

Corresponding author: Jian-xin XIE, Tel: +86-10-62332254, E-mail: jxxie@mater.ustb.edu.cn;
Lei JIANG, Tel: +86-13001114186, E-mail: leijiang@ustb.edu.cn
https://doi.org/10.1016/S1003-6326(25)66874-9

toughness. OHIRA and KISHI [12] reported a notable decrease in the fracture toughness of the 7075 Al alloy from 40 to 30 MPa·m$^{1/2}$ as the content of Fe went from 0 to 0.6 wt.%. VRATNICA et al [13] noticed that the higher content of Fe in the Al−Zn−Mg−Cu alloys resulted in a higher volume fraction of the secondary phases, which adversely impacted the ductility and fracture toughness. Furthermore, these Fe-rich phases are prone to crack initiation and facilitate crack propagation at their interfaces with the matrix under the applied stress [14]. These works have studied the impact of Fe and other alloying elements on the formation of coarse Fe-rich secondary phases in the 7xxx series aluminum alloys and their influence on properties. However, the impact of Fe on the formation and distribution of other secondary phases, as well as on the overall distribution of alloying elements within 7xxx series alloys remains unclear.

The microstructural details of the secondary phases are crucial to the properties of alloys [15−18]. The lattice of the microscale Fe-rich secondary phases is often incoherent with that of the Al matrix, therefore creating phase interfaces of high energy. These interfaces facilitate the accumulation and enrichment of elements such as Zn and Mg [19], thus altering the microstructures and properties. Furthermore, the excessive addition of other elements like Cr, Mn, Ti, and Zr can also induce the formation of secondary phases at the microscale [20]. Like Fe-rich secondary phases, these secondary phases would deteriorate properties in a similar way.

It is noted that all the alloys mentioned before share a commonality: the total amount of alloying elements is below 10 wt.%. To meet the ever pressing materials demands for lightweight aerospace components, we have developed an ultra-high strength Al alloy with remarkable toughness through machine learning [21,22]. This new alloy contains more than 14 wt.% of alloying elements. It maintains the ductility and toughness of the state-of-the-art 7136 alloy (elongation (δ) of 8%−10% and fracture toughness (K_{IC}) of 33−35 MPa·m$^{1/2}$) [23] while boosting up the tensile strength by over 100 MPa (700−750 MPa). However, the influence of Fe as an impurity element on the distribution of elements in ultra-high strength aluminum alloys remains obscure. This study concentrates on the study of the highly alloyed Al−10.50Zn−2.35Mg−1.25Cu−0.12Cr−0.1Mn−0.1Zr−0.1Ti−*x*Fe alloys (*x*=0.01, 0.09, 0.18, wt.%). We plan to analyze the impact of Fe on the microstructures, element distributions, and mechanical properties of the alloys. The work tries to elucidate the mechanisms how impurity elements influence the strength and toughness of the alloy, which would be insightful to further optimization of alloy compositions as well as the properties.

2 Experimental

Three alloys of different compositions were prepared via high-purity raw materials (99.99 wt.%) including Al, Zn, Mg, Mn, Cr, and intermediate alloys such as Al−50Cu, Al−10Ti, Al−10Zr, and Al−5Fe. The compositions of these alloys are detailed in Table 1. The raw materials were melted in a ZG−25 medium-frequency vacuum induction furnace and cast at 730−740 °C to produce several ingots. Ingots were cylindrical with a diameter of 125 mm, weighing 25 kg. Following casting, the ingots underwent a homogenization treatment in an SGM−M30/12A resistance furnace at 400 °C for 24 h, followed by an additional 24 h treatment at 470 °C. The ingots were then turn-milled, and the initial diameter of the extruded bar was set at 115 mm, with the extrusion barrel measuring 120 mm. The ingots were then extruded via a 500 t double-acting horizontal extrusion press at 400 °C and the extrusion ratio was 9:1.

Following extrusion, the bars underwent solid-solution treatments at 450 °C for 1 h, 470 °C for 1 h, and 480 °C for 0.5 h. Subsequently, the bars were aged at 120 °C for 24 h. Tensile specimens were then fabricated and tested at room temperature for their tensile strengths and elongations via a

Table 1 Alloy compositions (wt.%)

Alloy	Zn	Mg	Cu	Mn	Cr	Zr	Ti	Fe	Si	Al
0.01 wt.% Fe	10.53	2.38	1.24	0.11	0.13	0.11	0.10	<0.01	0.02	Bal.
0.09 wt.% Fe	10.52	2.33	1.27	0.11	0.12	0.10	0.09	0.09	0.02	Bal.
0.18 wt.% Fe	10.58	2.36	1.24	0.10	0.12	0.10	0.09	0.18	0.01	Bal.

CMT6000 testing machine with a strain rate of 0.5 mm/min. The specimens were prepared in a dog-bone shape with a gauge length of 20 mm and a cross-sectional area of 5 mm × 2 mm. The reported mechanical properties were averaged over two specimens.

Microstructure analysis was carried out with the Carl Zeiss EVO18 and JEOL JSM−7001F field emission scanning electron microscopes (SEM). Electron backscatter diffraction (EBSD) was performed at a 25 kV operating voltage to assess the grain morphology of the alloys, and the relevant data were analyzed with Channel 5 software from the University of Oxford. Additionally, high-angle annular dark-field (HAADF) imaging and compositional analysis were conducted at 300 kV using a Tecnai G2 F30 transmission electron microscope equipped with a HAADF detector and an energy-dispersive X-ray spectroscopy (EDS) system.

3 Results

3.1 Microstructures

The microstructures of the three Al alloys by SEM images are shown in Fig. 1. It is seen that the minimal amount of Fe in the Al−Zn−Mg−Cu alloy results in a scant formation of the microscale secondary phases, which roughly account for only 0.02% in volume fraction. As Fe goes up to 0.09 wt.%, the formation of these secondary phases is more pronounced, as evidenced by particles with an average diameter of (5.2±1.5) μm and a volume fraction of approximately 1.58%. As Fe continues to increase to 0.18 wt.%, an even higher volume fraction of these phases is noted, reaching 2.59%. The mean diameter of these secondary phases also grows to (13.6±3.2) μm. In addition, various microscale secondary phases with distinct shapes and sizes (some exceeding 30 μm) as well as black voids are noted to form.

Furthermore, the samples with 0.01 wt.% Fe and 0.18 wt.% Fe were selected to analyze the elemental distribution of the secondary phases at the microscale. Figure 2 presents the compositional analysis of these phases in the alloys with 0.01 and 0.18 wt.% Fe. In Fig. 2(a), the 0.01 wt.% Fe sample reveals a second phase enriched with Cr, Mn, and Mg, measuring approximately 5 μm in diameter. The compositional analysis, detailed in Table 2, suggests that this phase likely corresponds to $Al_{18}(Cr,Mn)_2Mg_3$. Additionally, surrounding this phase, an agglomeration of Zn, Mg, and Cu is observed.

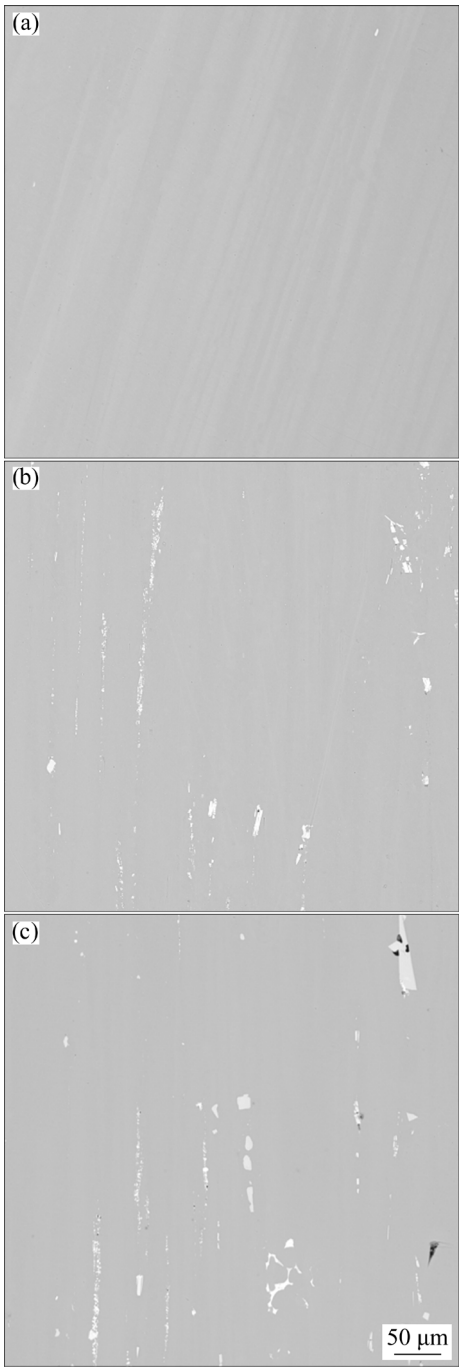

Fig. 1 SEM images of three ultra-high strength aluminum alloys with different Fe contents after T6 treatment: (a) 0.01 wt.% Fe; (b) 0.09 wt.% Fe; (c) 0.18 wt.% Fe

A considerable number of microscale secondary phases are shown in Fig. 2(b), predominantly constituted by the aggregation of Fe, Cu, Mn, and Cr. According to the compositional analysis

provided in Table 2, these phases likely correspond to (Cu,Fe,Mn,Cr)Al_7. In proximity to the microscale Fe-rich phases, there is a noticeable accumulation of Zn, Mg, and Cu, indicating the presence of the σ phase (composed of Al, Zn, Mg, and Cu). Additionally, the alloy contains microscale secondary phases composed of Cr, Mn, Zr, and Ti, such as $Al_{18}(Cr,Mn)_2Mg_3$ and $Al_3(Zr,Ti)$. Notably, $Al_3(Zr,Ti)$ is absent in the samples with 0.01 wt.% Fe.

Figures 3(a–c) illustrate grain morphologies of three alloys, all exhibiting extrusion texture and localized recrystallization. Figures 3(d–f) present the grain size statistics, indicating the average grain sizes of 7.0, 9.6, and 7.1 μm for the respective alloys.

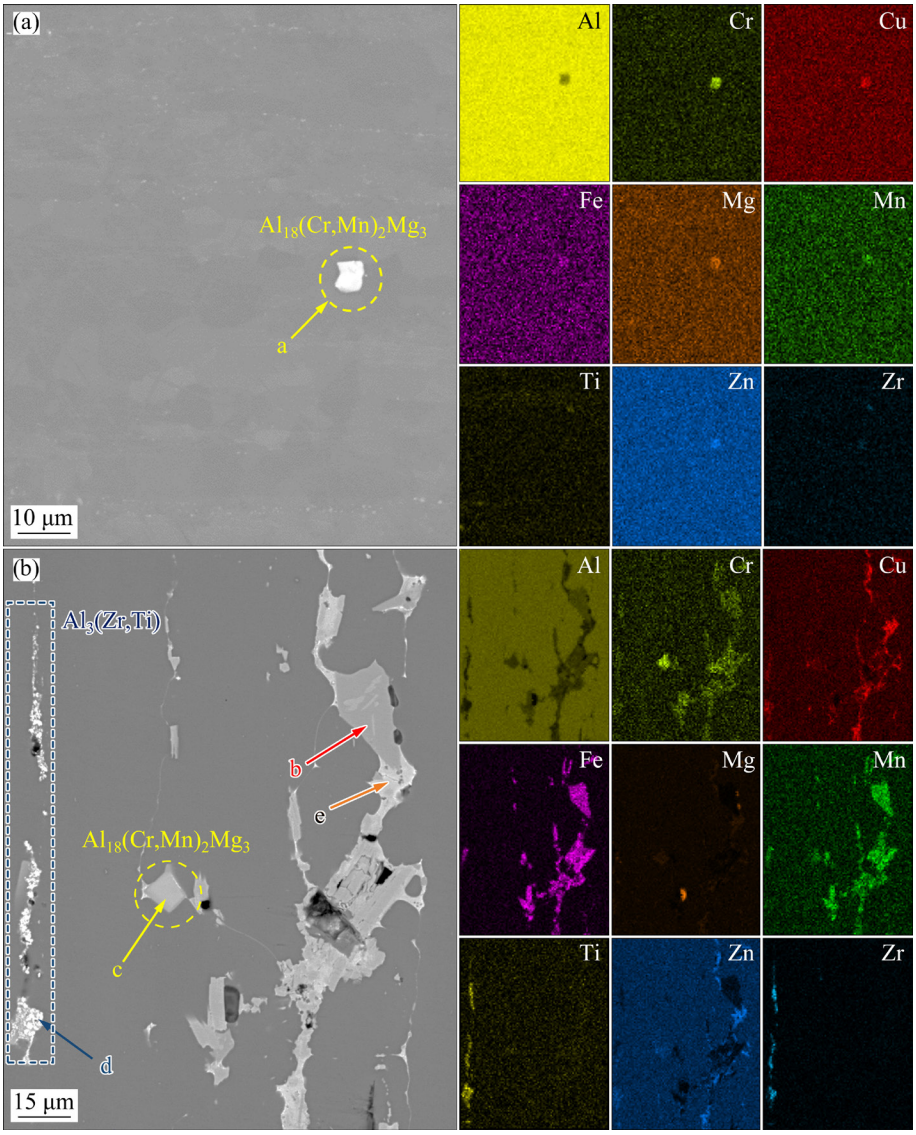

Fig. 2 Compositional analysis results of secondary phase: (a) 0.01 wt.% Fe; (b) 0.18 wt.% Fe

Table 2 EDS analysis results of arrowed locations in Fig. 2 (at.%)

Location	Al	Zn	Mg	Cu	Fe	Mn	Cr	Zr	Ti
a	80.62	4.21	7.51	2.05	0.01	2.38	3.12	0.06	0.04
b	83.07	2.46	1.46	2.27	9.00	1.33	0.40	0.00	0.00
c	80.47	3.72	6.91	1.83	0.05	2.45	3.60	0.00	0.00
d	71.72	5.49	6.10	2.14	0.03	0.06	0.10	6.46	6.50
e	83.11	8.09	6.09	2.61	0.03	0.00	0.03	0.00	0.03

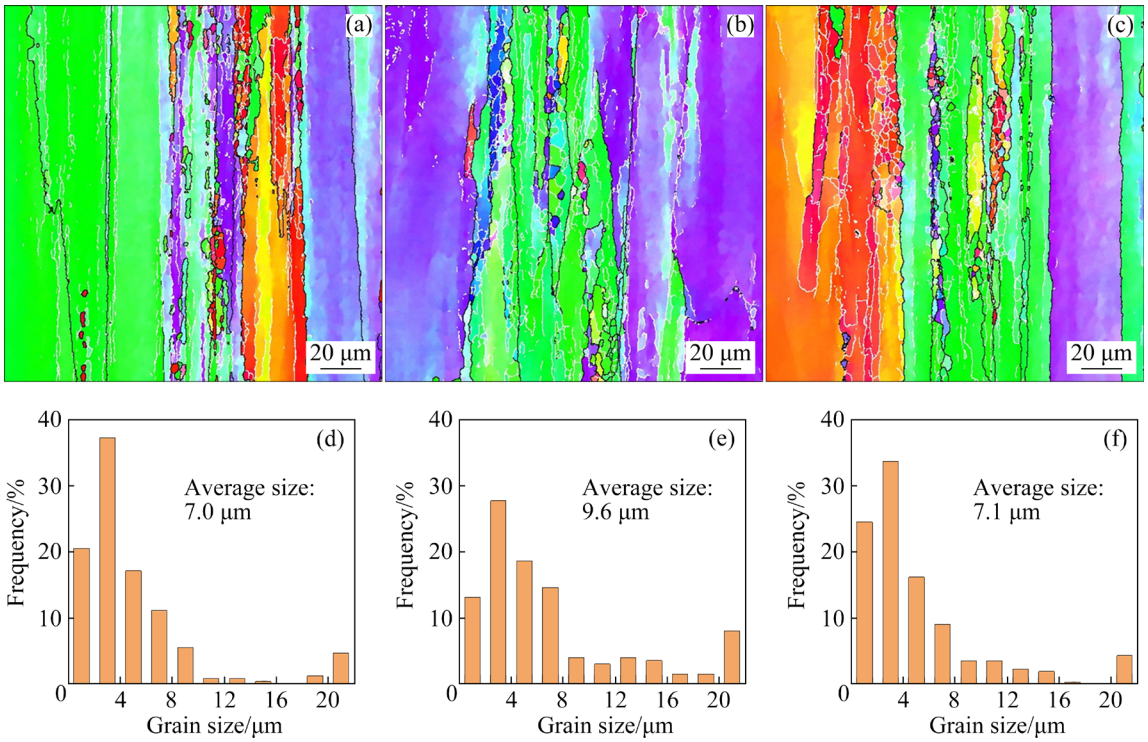

Fig. 3 EBSD results (a−c) and size statistics (d−f) for three alloys: (a, d) 0.01 wt.% Fe; (b, e) 0.09 wt.% Fe; (c, f) 0.18 wt.% Fe

The inclusion of Fe has a negligible impact on the grain size and the subtle variations in grain size may be associated with the uneven microstructure of alloy [24]. The microscale Fe-rich phase does not effectively induce particle simulated nucleation (PSN) nor refine the grain size.

Subsequently, the influence of Fe addition on the dispersion strengthening phases was investigated. Note that the dispersion strengthening phases can be categorized into two distinct types: dispersoids enriched with Cr, Mn, Zr, and Ti, and precipitates predominantly containing Zn, Mg, and Cu.

Figure 4 illustrates morphological distribution and compositional analysis results for typical dispersoids (i.e., secondary phases with diameters ranging from 20 nm to 1 μm) in the three alloys. These alloys feature multiple dispersoids composed of Cr, Mn, Zr, and Ti elements, with sizes varying from 20 to 300 nm. These dispersoids contribute to impeding grain boundaries and dislocations, thereby enhancing the strength of the alloy [21].

Additionally, the presence of Fe-rich phases significantly impacts the morphology of the dispersoids. Figure 5(a) demonstrates the influence of (Cu,Fe,Mn)Al_7 (length of 1.8 μm) on the morphology of the dispersoids. It can be seen that around the Fe-rich phase, there is a significant decrease in the number of dispersoids, with some areas even having no dispersoids whatsoever. As a result, some regions are depleted of solute elements such as Cr, Mn, Zr, and Ti. This effect extends up to a distance of 2−5 μm from the Fe-rich phase. In contrast, the nanoscale (Fe,Mn)Al_7 phases, approximately 500 nm in size, show no significant decrease in dispersoid quantity in their vicinity, as depicted in Fig. 5(b). This phenomenon may be attributed to their smaller dimensions, as nanoscale (Fe,Mn)Al_7 phases require fewer solute elements compared to their microscale counterparts. Furthermore, the nanoscale (Fe,Mn)Al_7 phases have a higher density and are more spherical in morphology compared to the microscale (Cu,Fe,Mn)Al_7 phases.

By further observation of the finer microstructures, the influence of Fe on the nanoscale precipitates composed of Zn, Mg, and Cu can be examined, as illustrated in Figs. 6(a–d). When there is insufficient Fe, the precipitates within the alloy have an average length of 4.9 nm and an average width of 2.3 nm. In the vicinity of the nanoscale Fe-rich phases, rich principal elements of Zn, Mg, and Cu are observed, which leads to the formation

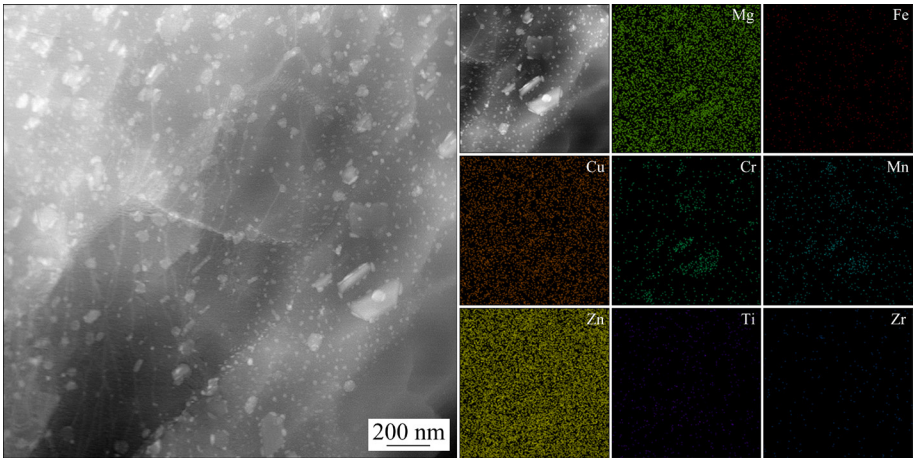

Fig. 4 HAADF-STEM image and composition analysis results of 0.18 wt.% Fe alloy after T6 treatment

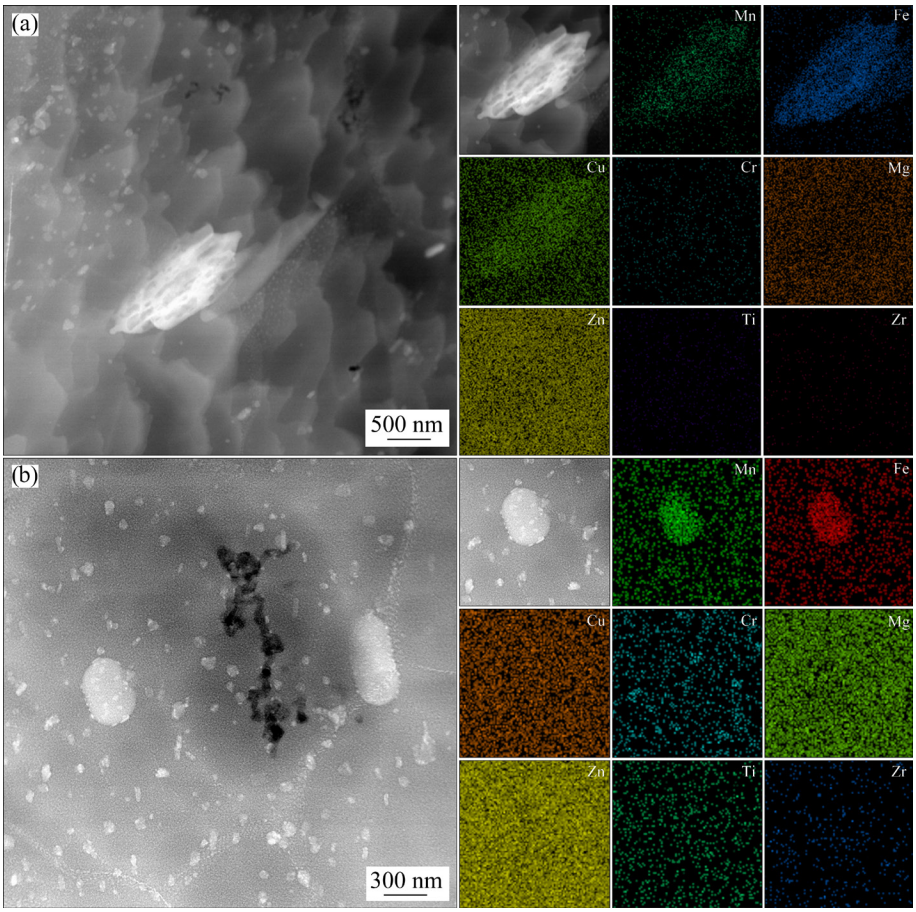

Fig. 5 HAADF-STEM images and composition analysis results of typical Fe-rich phases after T6 treatment in 0.18 wt.% Fe alloy: (a) Microscale Fe-rich phases; (b) Nanoscale Fe-rich phases

of larger η-phases. This phenomenon results in a significant reduction in the density of precipitates in the surrounding area, despite a solute deficiency. Additionally, despite the scarcity of solute elements, the average length of precipitates in the matrix near the Fe-rich phases measures 5.2 nm, and the average width is 2.5 nm. The presence of Fe slightly increases the size of precipitates compared to the condition when it is absent, which leads to a further decrease in the precipitate density. Moreover, analysis of the precipitates reveals that the addition of Fe does not alter the types of precipitates in the matrix. These phases still include η' phase, GP I, and GP II, as depicted in Figs. 6(e–g).

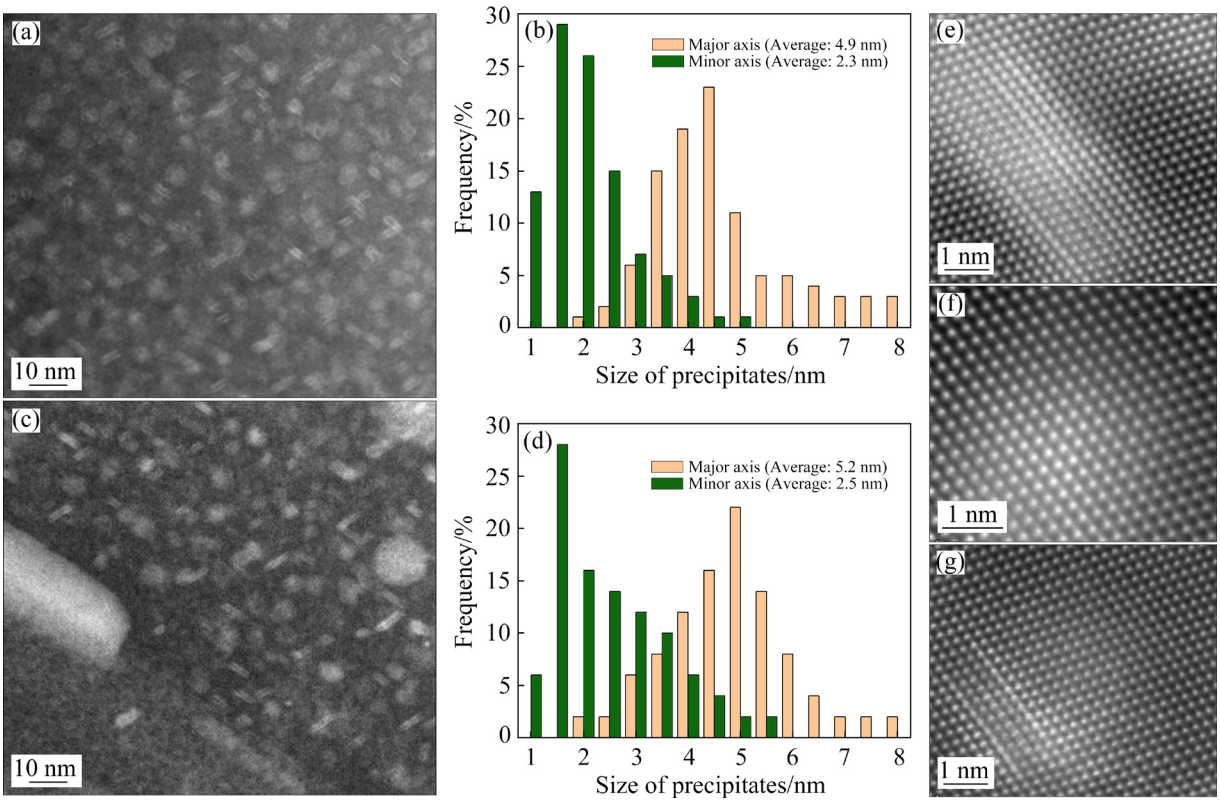

Fig. 6 High-resolution HADDF-STEM images (a, c) and size statistics (b, d) of precipitates without segregation (a, b) and precipitates under influence of segregation (c, d); HADDF-STEM images of η' phase (e), GP I (f) and GP II (g)

3.2 Mechanical properties

The outcomes of the tensile test of the three ultra-high strength Al alloys with different Fe contents are presented in Fig. 7 and Table 3. The tensile strengths of alloys measure (797±1) MPa, (785±9) MPa, and (788±8) MPa; their yield strengths are (762±1) MPa, (752±8) MPa, and (759±4) MPa; and elongations are (10.9±0.6)%, (9.9±0.3)%, and (4.5±1.4)%, respectively. The alloy with the lowest Fe content exhibits the highest tensile strength and elongation. When the Fe content increases to 0.09 wt.%, a slight reduction in both tensile strength and elongation is observed relative to alloy with 0.01 wt.% Fe. Further increasing the Fe content to 0.18 wt.% does not significantly alter the tensile strength, but leads to a reduction in elongation, decreasing it to less than half that observed in the alloys with 0.01 wt.% Fe.

In summary, the Fe content has a negligible effect on the strength of the high-strength Al−Zn−Mg−Cu alloys. When the Fe content is below 0.1 wt.%, its impact on the ductility of the alloys is minimal. However, with further increase in

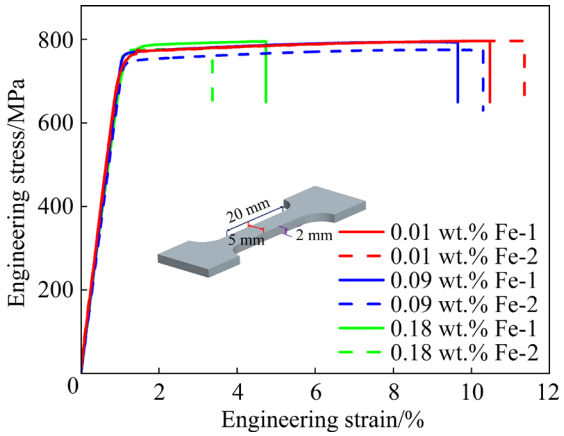

Fig. 7 Typical engineering stress−strain curves of three alloys

Table 3 Mechanical properties of three alloys

Alloy	Tensile strength/ MPa	Yield strength/ MPa	Elongation/ %
0.01 wt.% Fe	797±1	762±1	10.9±0.6
0.09 wt.% Fe	785±9	752±8	9.9±0.3
0.18 wt.% Fe	788±8	759±4	4.5±1.4

Fe content, there is a significant reduction in the ductility of the alloy.

4 Discussion

4.1 Effect of Fe on microscale secondary phases

Following the solution treatment and aging, the microscale secondary phases in the Al−10.50Zn−2.35Mg−1.25Cu−0.12Cr−0.1Mn−0.1Zr−0.1Ti alloy become virtually non-existent. Upon introducing Fe into the alloy, several microscale secondary phases, such as Fe-rich phases, σ phases, and $Al_3(Zr,Ti)$ phases, start coming into the scene.

To gain an in-depth understanding of the impact of Fe, thermodynamic calculations were performed using Thermo-Calc software with the TCAL6 Al alloy database. These calculations revealed variations in the volume fractions of phases with temperature for three levels of Fe contents (Fig. 8). As the Fe content increases, there is a gradual rise in the volume fraction of Fe-rich phases from 0 to 0.45%, corroborating the experimental observations of increased volume fractions of microscale Fe-rich secondary phases. Furthermore, the presence of Fe leads to an increase in the volume fraction of $Al_3(Zr,Ti)$ phases at 480 °C, which makes a complete solid solution of Ti and Zr in the matrix more challenging. On the other hand, the calculations indicate that the σ phases can completely dissolve at 480 °C.

At the peak solid-solution temperature of 480 °C, the maximum solubility of Fe in the alloy is below 0.01 wt.% [25]. Consequently, the gradual increase in the volume fraction of Fe-rich secondary phases can be attributed to the formation of phases as the Fe content increases [26]. The Fe-rich microscale secondary phases are notable for their incoherent interfaces with the Al matrix, characterized by higher interfacial energy. As a result, σ phases tend to segregate at interfaces, leading to the formation of microscale σ phases. Moreover, the originally homogeneous solid solution of Zr and Ti in the Al matrix results in the emergence of microscale second phase of $Al_3(Zr,Ti)$ with an increase in Fe content. This suggests that the presence of Fe elements decreases the maximum solubility of Zr and Ti in the Al matrix, thereby hindering their complete dissolving into the matrix at the elevated temperature of 480 °C. Consequently, residual $Al_3(Zr,Ti)$ microscale secondary

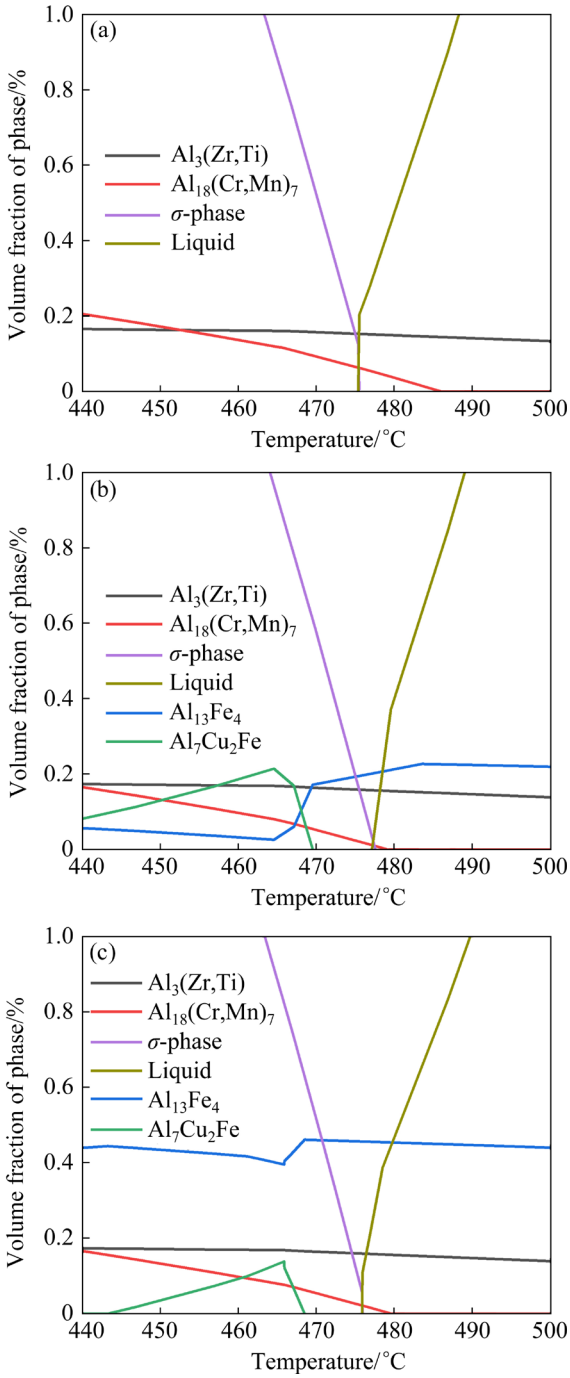

Fig. 8 Variation of volume fraction of phases in three ultra-high strength aluminum alloys with different Fe contents as function of temperature: (a) Fe-free; (b) 0.09 wt.% Fe; (c) 0.18 wt.% Fe

phases are formed. Regarding the formation of $Al_{18}(Cr,Mn)_2Mg_3$ phases, it is seen that even in the base alloy of Al−10.50Zn−2.35Mg−1.25Cu−0.12Cr−0.1Mn−0.1Zr−0.1Ti, a small amount of $Al_{18}(Cr,Mn)_2Mg_3$ phases are formed. This suggests that the formation of these phases may not be directly associated with the Fe-rich phases. It is also conceivable that the components of Fe-rich phases,

such as Cr and Mn, can potentially impede the formation of $Al_{18}(Cr,Mn)_2Mg_3$ phases.

4.2 Impact of Fe on strength and ductility of alloys

Fe, as an impurity element, may adversely affect the strength and ductility of the alloys. The Al−10.50Zn−2.35Mg−1.25Cu−0.12Cr−0.1Mn−0.1Zr−0.1Ti−*x*Fe alloys are designed to enhance strength through mechanisms such as precipitation strengthening, grain boundary strengthening, and solid-solution strengthening. The incorporation of Fe leads to the formation of microscale $(Cu,Fe,Mn,Cr)Al_7$ phases, depleting Cu, Mn, and Cr elements that tend to form dispersion-strengthening phases. Concurrently, the presence of Fe results in the segregation of primary elements such as Zn, Mg, and Cu at the boundaries of the $(Cu,Fe,Mn,Cr)Al_7$ phase, thereby diminishing the quantity of η', GP I, and GP II precipitation phases within the matrix. Additionally, the formation of microscale $Al_3(Zr,Ti)$ secondary phases contributes to the reduction in the number density of the nanoscale $Al_3(Zr,Ti)$ phases. Ultimately, the cumulative effects of these factors lead to a reduction in precipitation strengthening.

For grain boundary strengthening, the three alloys exhibit grain sizes of 7.0, 9.6, and 7.1 μm, respectively. According to the Hall−Petch equation ($\sigma_y=\sigma_0+k_y d^{-0.5}$) [27], where k_y equals 0.12 MPa·m$^{1/2}$, the calculated grain boundary strengthening values for these alloys are 45, 39, and 45 MPa, respectively. Notably, the alloy with 0.09 wt.% Fe shows reduced grain boundary strengthening effects. Concerning solid-solution strengthening, given that the primary compositions of the alloys are similar and their solution treatments and agings are identical, the relatively modest effect of solid-solution strengthening on the strength [21] suggests that substantial alterations of the solid-solution strengthening are unlikely.

In conclusion, the inclusion of Fe promotes the formation of coarse microscale secondary phases such as $(Cu,Fe,Mn,Cr)Al_7$, σ phase (composed of Al, Zn, Mg, and Cu elements), and $Al_3(Zr,Ti)$. Furthermore, this inclusion results in solute-depleted zones around Fe-rich phases, which significantly decreases the quantity of dispersion-strengthening phases and consequently reduces the effectiveness of precipitation strengthening. As a result, with increasing Fe content, the impact of precipitation strengthening gradually diminishes. The alloy with 0.09 wt.% Fe demonstrates reduced grain boundary strengthening effects, while the alloys with 0.01 and 0.18 wt.% Fe show similar effects. The influence of solid-solution strengthening is minimal. Consequently, the tensile strengths of the alloys measure (797±1), (785±9), and (788±8) MPa, respectively.

Regarding the ductility of the alloys, tensile test results indicate that the addition of 0.09 wt.% Fe has a minimal impact on ductility, resulting in a decrease in elongation from (10.9±0.6)% to (9.9±0.3)%. In these alloys, microscale Fe-rich phases exhibit an average diameter of (5.2±1.5) μm, featuring an elliptical morphology with a reduced number of adjacent voids. However, as the Fe content increases to 0.18 wt.%, ductility decreases to (4.5±1.4)%. There are microscale Fe-rich phases with an average diameter of (13.6±3.2) μm. Additionally, numerous sharp-edged microscale secondary phases greater than 30 μm in size are formed, accompanied by the emergence of black voids. Therefore, in manufacturing, regulating Fe content is crucial to preventing the formation of coarse Fe-rich phases and voids exceeding 30 μm in diameter.

Additionally, the presence of solute-depleted regions surrounding the Fe-rich microscale secondary phases significantly reduces the quantity of strengthening phases produced by Cr, Mn, Zr, and Ti. This phenomenon diminishes the strength of the matrix that encompasses micrometer-scale Fe-rich phases, making it more susceptible to void formation and cracking [28]. Although solute depletion near nanoscale Fe-rich phases is less pronounced, the segregation of Zn, Mg, and Cu still exists, resulting in reduced strength of the matrix. However, the impact on ductility is less significant compared to the microscale Fe-rich phases.

The microscale Fe-rich phases are inherently hard and brittle, and they exhibit poor compatibility with the matrix. Under low stress, these Fe-rich phases are prone to fracture or detachment from the substrate, forming voids that accelerate crack propagation [29−31]. Moreover, Fe-rich phases larger than 8 μm act as crack initiation sites, while the propensity for fracture in Fe-rich phases smaller

than 8 μm is significantly reduced [32]. In alloys containing 0.09 wt.% Fe, the average size of Fe-rich phases is (5.2±1.5) μm, while in those with 0.18 wt.% Fe, the average size is (13.6±3.2) μm. This variation also explains why the decrease in ductility is less significant in the alloys with 0.09 wt.% Fe.

5 Conclusions

(1) With increasing the Fe content, there is an increment in the volume fraction of the microscale phases, including (Cu,Fe,Mn,Cr)Al_7, σ phase (composed of Al, Zn, Mg, and Cu elements), and Al_3(Zr,Ti). The precipitation of these phases is accompanied by the formation of solute-depleted zones and the consumption of elements that form phases, which results in a significant reduction in the number of dispersion-strengthening phases.

(2) Fe has a minimal impact on the tensile strength of the alloy yet can significantly affect the elongation. The average elongation of the alloy with 0.18 wt.% Fe (δ=4.5%) is less than half that of the alloy with Fe less than 0.1 wt.% (δ=9.9%−10.9%). This reduction is attributed to the combined effects of microscale secondary phases and a substantial decrease in the number of dispersoids.

(3) The quantity of the precipitates decreases in the solute-depleted areas surrounding the Fe-rich phases, though the size of these phases remains largely unchanged.

CRediT authorship contribution statement

Xin-yuan XU: Data curation, Investigation, Writing – Original draft; **Lei JIANG:** Investigation, Conceptualization, Methodology, Writing – Review & editing; **Xin-biao ZHANG:** Investigation, Writing − Review & editing; **Ming-hong MAO:** Investigation, Writing − Review & editing; **Jian-xin XIE:** Conceptualization, Resources, Writing − Review & editing.

Declaration of competing interest

The authors declare that they have no known competing financial interests or personal relationships that could have appeared to influence the work reported in this paper.

Acknowledgments

This work was supported by the National Key Research and Development Program of China (No. 2023YFB3710501), the National Natural Science Foundation of China (No. 52401002), and the Beijing Municipal Science and Technology Commission, China (No. Z191100001119125).

References

[1] JAMSHIDI A H. Effects of aging heat treatment on microstructure and corrosion behavior of friction surfacing treated Al−Zn−Mg−Cu matrix composite [J]. Transactions of Nonferrous Metals Society of China, 2023, 33(8): 2303−2313.

[2] JUAN Yong-fei, NIU Guo-shuai, YANG Yang, XU Zi-han, YANG Jian, TANG Wen-qi, JIANG Hai-tao, HAN Yan-feng, DAI Yong-bing, ZHANG Jiao, SUN Bao-de. Accelerated design of Al−Zn−Mg−Cu alloys via machine learning [J]. Transactions of Nonferrous Metals Society of China, 2024, 34(3): 709−723.

[3] KAZEMI N A, JAMAATI R, JAMSHIDI A H. Effect of single roll drive rolling on microstructure, texture, and mechanical property anisotropy of Al−5.6Zn−2.5Mg−1.4Cu aluminum alloy [J]. Transactions of Nonferrous Metals Society of China, 2023, 33(11): 3266−3281.

[4] CVIJOVIĆ Z, RAKIN M, VRATNICA M, CVIJOVIĆ I. Microstructural dependence of fracture toughness in high-strength 7000 forging alloys [J]. Engineering Fracture Mechanics, 2008, 75(8): 2115−2129.

[5] ROBSON J D. Microstructural evolution in aluminium alloy 7050 during processing [J]. Materials Science and Engineering A, 2003, 382(1/2): 112−121.

[6] EIVANI A R, AHMED H, ZHOU J, DUSZCZYK J. Evolution of grain boundary phases during the homogenization of AA7020 aluminum alloy [J]. Metallurgical and Materials Transactions A, 2009, 40(3): 717−728.

[7] SHA G, WANG Y B, LIAO X Z, DUAN Z C, RINGER S P, LANGDON T G. Microstructural evolution of Fe-rich particles in an Al−Zn−Mg−Cu alloy during equal-channel angular pressing [J]. Materials Science and Engineering A, 2010, 527(18/19): 4742−4749.

[8] ANDREATTA F, TERRYN H, WIT J H W D. Effect of solution heat treatment on galvanic coupling between intermetallics and matrix in AA7075–T6 [J]. Corrosion Science, 2003, 45(8): 1733−1746.

[9] GAO M, FENG C R, WEI R P. An analytical electron microscopy study of constituent particles in commercial 7075−T6 and 2024−T3 alloys [J]. Metallurgical and Materials Transactions A, 1998, 29(4): 717−728.

[10] ZHANG Meng-han, LIU Sheng-dan, JIANG Jing-yu, WEI Wei-chang. Effect of Cu content on intergranular corrosion and exfoliation corrosion susceptibility of Al−Zn−Mg−(Cu) alloys [J]. Transactions of Nonferrous Metals Society of China, 2023, 33(7): 1963−1976.

[11] FENG Xin-ming, WANG Zhi-lei, JIANG Lei, ZHAO Fan,

ZHANG Zhi-hao. Simultaneous enhancement in mechanical and corrosion properties of Al−Mg−Si alloys using machine learning [J]. Journal of Materials Science & Technology, 2023, 167: 1−13.

[12] OHIRA T, KISHI T. Effect of iron content on fracture toughness and cracking processes in high strength Al−Zn−Mg−Cu alloy [J]. Materials Science and Engineering, 1986, 78(1): 9−19.

[13] VRATNICA M, PLUVINAGE G, JODIN P, CVIJOVIĆ Z, RAKIN M, BURZIĆ Z. Influence of notch radius and microstructure on the fracture behavior of Al−Zn−Mg−Cu alloys of different purity [J]. Materials & Design, 2010, 31: 1790−1798.

[14] YAN L, FAN J K. In-situ SEM study of fatigue crack initiation and propagation behavior in 2524 aluminum alloy [J]. Materials & Design, 2016, 110: 592−601.

[15] CHEN Yu-meng, WU Yu-na, GENG Jun, LIU Huan, SONG Dan, JIANG Jing-hua, FANG Feng, MA Ai-bin. Pre-precipitating promoted by microshear bands effectively circumvents strength-ductility trade-off of RT-rolled Al−6Zn−1Mg alloy [J]. Journal of Materials Research and Technology, 2024, 28: 2767−2777.

[16] YUAN Ding-ling, CHEN Song-yi, CHEN Kang-hua, HUANG Lan-ping, CHANG Jiang-yu, ZHOU Liang, DING Yun-feng. Correlations among stress corrosion cracking, grain-boundary microchemistry, and Zn content in high Zn-containing Al−Zn−Mg−Cu alloys [J]. Transactions of Nonferrous Metals Society of China, 2021, 31(8): 2220−2231.

[17] XU Rui, LIN Bo, LI Hao-yu, XIAO Hua-qiang, ZHAO Yu-liang, ZHANG Wei-wen. Microstructure evolution and mechanical properties of Al−6.5Cu−0.6Mn−0.5Fe alloys with different Si additions [J]. Transactions of Nonferrous Metals Society of China, 2019, 29(8): 1583−1591.

[18] JIANG Lei, FU Hua-dong, WANG Chang-sheng, LI Wei-dong, XIE Jian-xin. Enhanced mechanical and electrical properties of a Cu−Ni−Si alloy by thermo-mechanical processing [J]. Metallurgical and Materials Transactions A, 2020, 51(1): 331−341.

[19] XIAO Hong-yu, LI Yu-gang, GENG Ji-wei, LI Hong-ping, WANG Ming-liang, CHEN Dong, LI Zhu-guo, WANG Hao-wei. Effects of nano-sized TiB_2 particles and Al_3Zr dispersoids on microstructure and mechanical properties of Al−Zn−Mg−Cu based materials [J]. Transactions of Nonferrous Metals Society of China, 2021, 31(8): 2189−2207.

[20] FANG Hua-chan, YANG Hai-lin, ZHU Jia-min, XIAO Peng, CHEN Zhuo, LIU Tan. Effect of minor Cr, Mn, Zr or Ti on recrystallization, secondary phases and fracture behaviour of Al−Zn−Mg−Cu−Yb alloys [J]. Rare Metal Materials and Engineering, 2020, 49(3): 797−810.

[21] JIANG Lei, WANG Chang-sheng, FU Hua-dong, SHEN Jie, ZHANG Zhi-hao, XIE Jian-xin. Discovery of aluminum alloys with ultrastrength and high-toughness via a property-oriented design strategy [J]. Journal of Materials Science & Technology, 2022, 98: 33−43.

[22] JIANG Lei, ZHANG Zhi-hao, FU Hua-dong, HUANG Shi-yu, ZHUANG Da-wei, XIE Jian-xin. Corrosion behavior and mechanism of Al−Zn−Mg−Cu alloy based on the characterization of the secondary phases [J]. Materials Characterization, 2022, 189: 111974.

[23] JIANG Lei, FU Hua-dong, ZHANG Zhi-hao, ZHANG Hong-tao, ZHANG Xin-biao, FENG Xin-ming, XU Xin-yuan, MAO Ming-hong, XIE Jian-xin. Synchronously enhancing the strength, toughness, and stress corrosion resistance of high-end aluminum alloys via interpretable machine learning [J]. Acta Materialia, 2024, 270: 119873.

[24] ZHAO Zi-yao, XIAO Na-min, ZHANG Zhi-hao, WANG Zhi-lei. Improved stress relaxation stability of a heat-resistant Al−Cu−Mg−Ag alloy with good mechanical properties by a pre-annealing/solution-aging treatment [J]. Journal of Alloys and Compounds, 2023, 961: 171145.

[25] HAN K, OHNUMA I, KAINUMA R. Experimental determination of phase equilibria of Al-rich portion in the Al−Fe binary system [J]. Journal of Alloys and Compounds, 2016, 668: 97−106.

[26] WEN K, XIONG B Q, REN W C. Fe-rich particles influenced secondary crack characteristics in an Al−Zn−Mg−Cu alloy extrusion plate with high zinc content [J]. Scripta Materialia, 2020, 186: 259−262.

[27] JIANG Lei, FU Hua-dong, ZHANG Hong-tao, XIE Jian-xin. Physical mechanism interpretation of polycrystalline metals' yield strength via a data-driven method: A novel Hall−Petch relationship [J]. Acta Materialia, 2022, 231: 117868.

[28] JIANG Lei, ZHANG Zhi-hao, HU Hao, HE Xing-qun, FU Hua-dong, XIE Jian-xin. A rapid and effective method for alloy materials design via sample data transfer machine learning [J]. NPJ Computational Materials, 2023, 9: 26.

[29] NADIM A, TAGHIABADI R, RAZAGHIAN A, NOGHANI M T, GHONCHEH M H. Effect of Fe-impurity on tribological properties of Al−15Mg_2Si composite [J]. Transactions of Nonferrous Metals Society of China, 2018, 28(6): 1084−1093.

[30] MORGENEYER T F, STARINK M J, SINCLAIR I. Evolution of voids during ductile crack propagation in an aluminium alloy sheet toughness test studied by synchrotron radiation computed tomography [J]. Acta Materialia, 2008, 56: 1671−1679.

[31] HU Ke, LIN Chi-hao, XIA Song-chao, ZHENG Cheng-kun, LIN Bo. Effect of Fe content on low cycle fatigue behavior of squeeze cast Al−Zn−Mg−Cu alloys [J]. Materials Characterization, 2020, 170: 110680.

[32] JIAN Hai-gen, JIANG Feng, WEN Kang, JIANG Long, HUANG Hong-feng, WEI Li-li. Fatigue fracture of high-strength Al−Zn−Mg−Cu alloy [J]. Transactions of Nonferrous Metals Society of China, 2009, 19(5): 1031−1036.

铁含量对新型超高强 Al−Zn−Mg−Cu 合金显微组织与力学性能的影响

许心渊[1]，姜 磊[1]，张鑫彪[1]，毛铭宏[1]，谢建新[1,2,3]

1．北京科技大学 北京材料基因工程高精尖创新中心，北京 100083；
2．北京科技大学 现代交通金属材料与加工技术北京实验室，北京 100083；
3．北京科技大学 材料先进制备技术教育部重点实验室，北京 100083

摘 要：研究了铁含量对 Al−10.50Zn−2.35Mg−1.25Cu−0.12Cr−0.1Mn−0.1Zr−0.1Ti 超高强铝合金显微组织与力学性能的影响。结果表明，Fe 含量的增加使得微米级第二相如(Cu,Fe,Mn,Cr)Al_7 相、σ 相(由 Al、Zn、Mg 和 Cu 元素组成)和 Al_3(Zr,Ti)相的体积分数显著增加，导致强化相形成元素的消耗，从而使得强化相的数量显著减少。虽然铁元素对抗拉强度的影响较小，但它显著影响伸长率(δ)。例如，含 0.18%(质量分数)Fe 的合金其平均伸长率(δ=4.5%)不足 Fe 含量<0.1%(质量分数)合金的一半(δ=9.9%~10.9%)。这种减少归因于粗大第二相的形成和第二相周围强化相数量减少的综合作用。

关键词：Al−Zn−Mg−Cu 合金；拉伸性能；元素分布；第二相；Fe 含量

(Edited by Bing YANG)